Understanding the circulation in the deep, micro-tidal and strongly stratified Congo River estuary

Valentin Vallaeys [a],[*], Jonathan Lambrechts [b], Philippe Delandmeter [b], Johannes Pätsch [c],[d], Alejandro Spitzy [e], Emmanuel Hanert [a],[b], Eric Deleersnijder [b],[a]

[a] *Université catholique de Louvain, Earth and Life Institute (ELI), Louvain-la-Neuve, Belgium*
[b] *Université catholique de Louvain, Institute of Mechanics, Materials and Civil Engineering (IMMC), Louvain-la-Neuve, Belgium*
[c] *Universität Hamburg, Institute of Oceanography, Hamburg, Germany*
[d] *Helmholtz-Zentrum Geesthacht, Institute of Coastal Research, Geesthacht, Germany*
[e] *Universität Hamburg, Institute of Geology, Hamburg, Germany*

ARTICLE INFO

ABSTRACT

The Congo River estuary is characterised by a deep canyon that connects the river to the deep ocean by cutting through the continental shelf. Its estuary is influenced by high river discharge and micro-tidal conditions, with a large depth and limited vertical mixing. This restricts the supply of oxygen from the surface waters to the more saline bottom waters, leading to hypoxic and anoxic zones. We study the dynamics of the Congo River estuary by applying the multi-scale baroclinic coastal ocean model SLIM 3D (www.slim-ocean.be) to this topographically challenging environment. By allowing a high degree of flexibility in the representation of both the complex geometry and the strong stratification, SLIM 3D is able to simulate riverine, tidal and gravitational processes that drive the estuarine circulation. Model results compare favourably with in-situ data in the estuary, suggesting that the exchange flow is correctly simulated. The latter is characterised by a two-layer dynamics. The combination of the large river discharge, the strong stratification and the large depth results in a moderate freshwater Froude number and a very small mixing number. It makes the Congo River an outlier in state-of-the-art estuarine classifications, closer to fjords than salt wedge estuaries. Furthermore, using the age as a diagnosis sheds light on the spatial variability of the estuarine waters ventilation. Local maximum of renewing water age located just below the pycnocline is exceeded by old dense oceanic waters which stagnate at the bottom of the canyon for more than two months due to the small vertical mixing. It helps explain the hypoxic and anoxic conditions observed at the bottom of the submarine canyon.
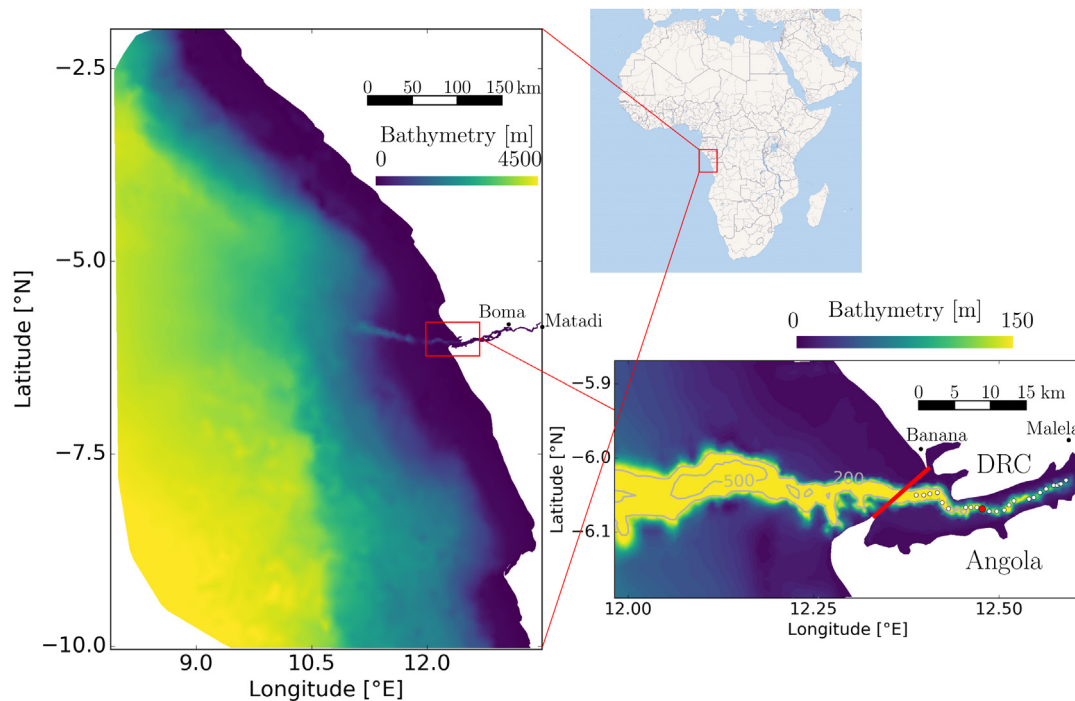
1. Introduction

The Congo River is the main African freshwater input into the Atlantic Ocean. With a watershed of 3.7×10^6 km^2 and a mean river discharge of about 4×10^4 m^3/s, second only to the Amazon River, the Congo strongly affects the sea surface salinity in the Eastern Atlantic Ocean (Vangriesheim et al., 2009). Pak et al. (1984) reported that its plume forms a surface lens that extends 800 km offshore, reaching latitude 8° East. This large outflow transports a large amount of suspended matter into the Atlantic Ocean (Eisma et al., 1978). In Kinshasa, located 300 km upstream of the estuary, the total suspended sediment flux reaches 30.7×10^6 tons/year, and approximately 6% of it is particulate organic carbon (POC) (Coynel et al., 2005). Only half of the POC gravitationally settles into the subhalocline water body of the canyon, the other half being advected offshore with the surface plume (Eisma and Kalf, 1984). Hence the Congo River plays an

important role for the local, regional and global carbon fluxes at the land–ocean interface.

Despite the importance of the Congo River, there are very few publications about the hydrodynamics of the Congo's estuary and region of freshwater influence (ROFI). Hopkins et al. (2013) and Chao et al. (2015) tracked the plume by means of satellite data products. The first numerical model of the plume dynamics was set up by Denamiel et al. (2013), using ROMS (Shchepetkin and McWilliams, 2005). They studied the impact of topographic features, in particular the submarine canyon, and variable forcings on the plume movement. The model was further used to investigate the influence of the outflow on the sea surface temperature in the near shore region (White and Toumi, 2014), and the relevance of data assimilation in the regional-scale modelling of this area (Phillipson and Toumi, 2017, 2019). As these studies focused on the freshwater plume, the computational domains did not include the Congo River itself. To the best of our knowledge, the only numerical

Fig. 1. Bathymetry of the domain of interest (left) with a focus on the estuary (right). The submarine canyon is clearly visible: its depth reaches more than 250 m at the mouth and 100 m at its upstream head. The white dots in the close-up view (lower right panel) represent the stations where data profiles are available. The red dot is the location where vertical mean profiles are computed. The red line represents the open boundary to be used for calculating the renewing water age (Section 2.3). DRC is the acronym for Democratic Republic of the Congo.

study of the whole tidally-influenced Congo River has been conducted by Le Bars et al. (2016) by means of a depth-averaged barotropic model, which, by construction, could not deal with the baroclinic aspects of the flow.

The deep submarine canyon – one of the largest in the world – that directly connects the ocean with the lower estuary impacts the plume and shelf dynamics as well as the estuarine circulation. The large variations of the water column depth and the steep bathymetry gradients, with slopes up to 50%, imply that the numerical grid of any numerical model of this region must be designed with care. It is desirable that the "hydrostatic consistency criterion"[1] (Haney, 1991) be met so as to avoid significant errors in the evaluation of the discrete pressure force, requiring the implementation of a flexible horizontal resolution and a suitable vertical coordinate system (Haney, 1991; Deleersnijder and Beckers, 1992; Burchard and Beckers, 2004; Hofmeister et al., 2010; Berntsen, 2011; Zhang et al., 2015; Li et al., 2016). Furthermore, the strong stratification inside the estuary requires low numerical dissipation schemes. Clearly, modelling the barotropic and baroclinic circulation along the Congo river-to-sea continuum represents a challenging test case for any numerical model.

Since Hansen and Rattray (1966), estuarine classification into different regimes has been an active field of study (see for example Geyer and MacCready, 2014, and references therein). As the discharge and the tides change over time, an estuary may switch from one regime to another one, as exemplified by the Columbia River estuary (Kärnä and Baptista, 2016a). In many estuaries, vertical mixing is mostly driven by the tides. The Congo River estuary is micro-tidal, with a tidal range varying between 1.9 m during spring tides and 0.3 m during neap tides at the river mouth, near Banana (see Fig. 1 for the exact location) (Eisma and van Bennekom, 1978). In combination with the large depth of the canyon, the regime of the Congo River estuary is

thus expected to be classified as a strongly stratified estuary, mostly driven by salinity differences. Such estuarine feature is often associated with low-discharge estuaries or fjords. However, unlike such small-velocity systems, the Congo estuary is driven by a huge and stable water discharge that produces a large and steady mean river velocity. As such, it appears as a very peculiar estuary, which is likely to be an outlier in estuarine classifications.

Another salient feature of the Congo estuary is the presence of vast hypoxic and anoxic zones. Because of the mineralisation of POC in sinking sediments, the dissolved oxygen concentration steadily decreases below the freshwater surface layer. This is enhanced by stratification that reduces the vertical mixing below the pycnocline. Low-oxygen zones have been reported in the deep estuary, with an oxygen concentration that almost vanishes near the bottom (Eisma and van Bennekom, 1978). This has qualitatively been understood but not yet quantified in detail for the Congo River (van Bennekom et al., 1978). Similar hypoxic conditions are reported for the Neuse River (Paerl et al., 1998) or Puget Sound (Feely et al., 2010), although they exhibit large seasonal variations.

The goal of this paper is to advance our understanding of the Congo River estuarine dynamics by applying the multi-scale hydrodynamic model SLIM 3D [2] to the Congo river-to-sea continuum. SLIM 3D is an unstructured-mesh, discontinuous Galerkin model that is well suited to simulate flows in topographically-challenging areas. After being compared with field observations, the model is used to study the 3D flow structure within this estuary. That allows us to assess the importance of tidal mixing and stratification and hence position the Congo River in Geyer and MacCready (2014)'s estuarine classification. By further coupling the hydrodynamic model with a renewing water

---

[1] As was argued by Deleersnijder (2015), this criterion has little to do with the consistency of the numerical scheme *per se* and instead is closely related to the accuracy of the discretisation of the horizontal pressure force term.

[2] SLIM: Second-generation Louvain-la-Neuve Ice-ocean Model, www.slim-ocean.be

age diagnostic tool, we can show how the combination of a large depth, weak tide and high discharge leads to very slow water renewal at the bottom of the estuary, which in turn leads to hypoxic conditions.

The paper is organised as follows. Section 2 details the methods and data, i.e. the available in situ observations, the numerical model and the diagnostic tools. The results are presented in Section 3: the model reference run is compared against field data in Section 3.1; insights into the estuarine classification (resp. circulation) are provided in Section 3.2 (resp. 3.3); renewing water age theory is applied to the estuary in Section 3.4; a schematic oxygen budget is outlined in Section 3.5. Finally, results are discussed in Section 4. Conclusions are drawn in the same section.

2. Methods and data

2.1. In-situ measurements

About thirty years ago, Eisma (1990) collected data along the Congo River canyon (Fig. 1). While navigating, measurements of salinity, temperature and oxygen were made at different locations (represented with white dots in Fig. 1) and at different depths. These data were collected from November 21th 1989 for the upstream river, until December 12th 1989 for the oceanic measurements. In the estuary, measurements were performed from 27 November to 30 November. Since they were taken "along the way", the atmospheric and oceanic conditions were not constant during the measurement period. The measured estuarine profiles of salinity, temperature and oxygen are shown in Fig. 2.

The observed salinity and temperature profiles show the high vertical stratification of the Congo River estuary. The pycnocline is located at a depth of about 10 m. The freshwater layer thickness is almost constant in the whole transect, except at the plume lift-off near the mouth where the layer is thinner. The vertical stratification is strong, with salinity differences of 35×10^{-3} within 5 m. These observations are consistent with those of Spencer et al. (2013), who mentioned the presence of very saline water ($>35 \times 10^{-3}$) just downstream of Malela under a 10 m freshwater surface layer, and a plume thickness of about 2-3 m at the mouth with surface salinity near zero. The stratification is mostly controlled by salinity differences and seems to be rather insensitive to tidal motions.

Oxygen concentrations show a strong vertical variability, with relatively high oxygen concentrations located near the surface and large areas of hypoxia (<187.5 mmol O_2 m^{-3}, dashed line in Fig. 2), and even anoxia (<62.5 mmol O_2 m^{-3}, solid line in Fig. 2), in the bottom layer of the estuary. There is a clear similarity between the salinity, temperature and oxygen profiles.

For context, Fig. 3 shows seasonal variations of river discharge (at Matadi) and tidal elevation (at Banana, near the river mouth). The analysis period (dark grey) is in the wet Austral summer. The river discharge is large throughout the year and varies between 2 and 7×10^4 m^3/s. December generally features the highest river discharge, with a mean value around 5.5×10^4 m^3/s. Fresh water discharge of December 1989 was slightly smaller than the seasonal mean but remains above yearly average values.

2.2. Model setup

The three-dimensional hydrodynamics is simulated by means of the baroclinic ocean model SLIM 3D (Kärnä et al., 2013; Delandmeter et al., 2015, 2018; Vallaeys et al., 2018). It solves the 3D hydrostatic equations under the Boussinesq approximation on an unstructured mesh by means of the discontinuous Galerkin (DG) finite element method (Blaise et al., 2010). SLIM 3D has recently been used to simulate the thermocline oscillations in Lake Tanganyika with a vertically adaptive grid (Delandmeter et al., 2018), the coupled estuarine-plume dynamics of the Columbia River (Vallaeys et al., 2018) and the algal bloom occurrence in Lake Titicaca (Duquesne et al., 2021). The model is run from 15 August 1989 until 1 January 1990. The model spin up lasts until the analysis starts, on 1 November. We then compare the simulated results with the observations of Eisma (1990).

2.2.1. 3D Baroclinic model

The model equations are described in Delandmeter et al. (2018). They are based on a formulation that preserves tracer consistency (White et al., 2008) at a discrete level (Delandmeter et al., 2018). Such a formulation ensures an accurate coupling between the hydrodynamical and tracer transport modules. DG methods scale well on parallel computer platforms thanks to their spatial sparsity. They also offer functional flexibility as the model solutions can be discontinuous between mesh elements. This is particularly useful for modelling flows in topographically challenging environments. In the case of the Congo River, the sides of the submarine canyon that cut through the continental shelf are so steep that it is almost impossible to achieve a mesh fine enough to represent them accurately. As a result, the model has to be flexible enough to deal with under-resolved topographic features without resorting to unphysical dissipation. The DG formulation allows SLIM 3D to handle strong gradients of bathymetry, density and velocity with little numerical dissipation, as shown in Vallaeys et al. (2018).

2.2.2. Computational domain

The domain of interest covers the Atlantic Ocean near the Congo River mouth, from 2° S to 10° S, and from 8° E to the African west coast. At the border between Angola and Democratic Republic of Congo (DRC), at approximately 6° S, the domain includes the whole tidally influenced Congo River, from Banana at the mouth to Matadi, about 150 km upstream of it (Fig. 1). The latter area is separated from the capital of DRC, Kinshasa, by rapids flowing over about 290 km.

The water depth ranges from more than 4500 m in the deep ocean to a few metres in the estuary (Fig. 1). The computational bathymetry has been obtained by merging the global data from GEBCO 2008 (Monahan, 2008) with digitalised nautical charts of the river (Le Bars et al., 2016). The bathymetry features of the Congo River estuary are shown in Fig. 1. A deep canyon (depth > 250 m) splits the Congo River estuary into two distinct parts. The submarine canyon originates from the post-rift evolution of the continental margin of west-equatorial Africa (Savoye et al., 2009). Shallow zones (depth < 20 m) are found along both sides of the estuarine canyon with half of the non canyon area shallower than 10 m.
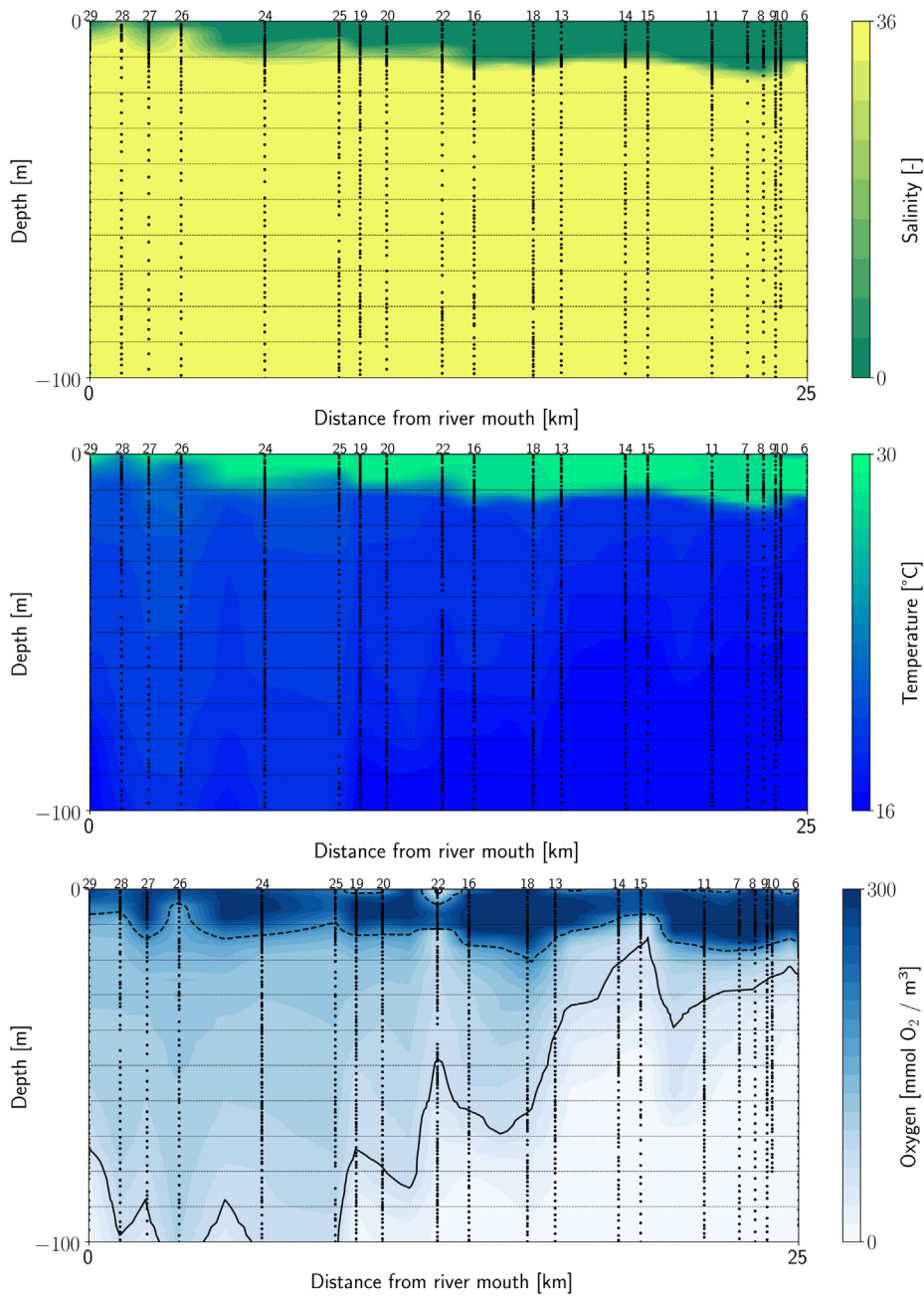
The estuary is characterised by a number of channels between Boma and Malela. Downstream of this region, mangroves occupy large shallow areas on each bank. As only very little topographical information is available for those areas, they are left out of the domain. A minimal depth of 3 m is prescribed as wetting and drying processes are not explicitly taken into account, as in Vallaeys et al. (2018).

2.2.3. Mesh generation

Owing to the specific nature of the domain of interest (rugged bathymetry, wide range of characteristic length scales), mesh generation is crucial (Lambrechts et al., 2008). Clearly, the horizontal mesh size must be sufficiently small in the estuary and in the vicinity of the coast, and can be significantly larger in the deep ocean. Then, in the region where the bottom slope is the steepest, in particular along the sides of the canyon, the horizontal mesh resolution must be further enhanced. Special attention must also be devoted to the determination of the vertical grid size, with a finer mesh where vertical gradients of density and velocity are highest (near the top surface of the water column inside the estuary for example).

As in other previous applications of SLIM 3D , we resort to a two-stage mesh generation procedure (see for example Delandmeter et al., 2015). First, a triangular unstructured surface mesh is generated by means of GMSH (http://gmsh.info) (Geuzaine and Remacle, 2009). Then, this mesh is extruded along the vertical direction, yielding prismatic elements. Here we use a hybrid σ–z vertical grid with σ levels near the surface and z levels below the transition depth h_σ, as in Vallaeys et al. (2018). This type of mesh facilitates the representation of the hydrostatic equilibrium, especially with low-order discretisations.
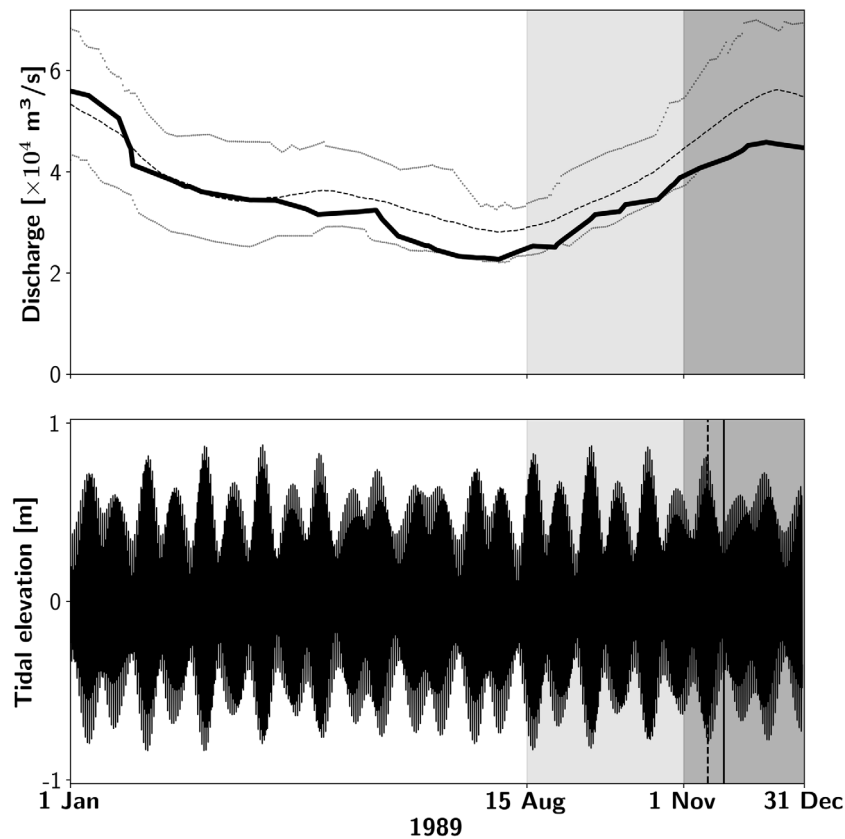
Fig. 2. From top to bottom, vertical profiles of observed salinity, temperature and oxygen in the Congo River canyon in November–December 1989 (Eisma, 1990). Profiles are reconstructed by interpolating vertical observations at each station. The ocean (resp. river) is on the left (resp. right) hand side. The horizontal axis represents the distance to the river mouth (measured in the upstream direction) along the transect delineated by the stations shown in white dots in Fig. 1. There is a sharp pycnocline whose depth barely exceeds 15 m. Hypoxic (dashed line) and anoxic (solid) limits are highlighted in the lower panel.

The surface mesh consists of about 1.6×10^4 triangles. The reference element mesh size of the horizontal triangles is set to the minimum of two linear functions of the distance to the continental and estuarine coastlines. The reference mesh size reaches 500 m along the banks of the estuary and 3 km near the other coastlines. It further decreases to reach a mesh size of 15 km at 50 km from the coast, in the deepest parts of the domain (Fig. 4).

Next, seeking inspiration in Haney (1991), Deleersnijder and Beckers (1992) and Legrand et al. (2007), a horizontal length characterising the bottom topography is evaluated, namely $L_h = \frac{h}{|\nabla_h h|}$, where h and ∇_h denote the unperturbed height of the water column and the horizontal gradient operator, respectively. The objective is to further refine the surface mesh in such a way that this length is resolved. However, this would lead to a significant increase in the number of

elements. Therefore, using the method of Legrand et al. (2007), we generate anisotropic elements, whose size is smaller in the direction of the bathymetry gradient than in the orthogonal direction with a maximum mesh size of 300 m. The anisotropic mesh has about half the number of elements than an isotropic mesh would have. In other words, length scale L_h is still resolved, albeit in a directional manner.

The surface mesh is finally vertically extruded to form prisms. The anisotropic mesh is extruded with $h_\sigma = 12$ m and is made up of 5 σ layers on top of at most 27 z layers. The value of h_σ has been obtained following a calibration procedure with respect to a high resolution reference solution. The 5 uppermost σ levels have a maximal depth of 1, 3, 5, 8 and 12 metres below sea level to increase the near-surface resolution. As soon as depth exceeds 14 m, a number of z levels is added below the σ levels, at depths 16, 20, 25, 30, 35, 40,

Fig. 3. Time evolution of the Congo River discharge (top) and tidal elevation at the river mouth (bottom) throughout the entire year 1989. The river discharge (solid line) is compared with the mean (dashed) and min/max (dotted) values over the period 1981–2010. The simulation and analysis periods are shown in light and dark grey, respectively. The latter is entirely included within the former. Vertical lines in the bottom panel represent the spring (dashed) and neap (solid) time stamps used for the analysis.

45, 50, 60, 70, 80, 90, 100, 120, 150, 175, 200, 250, 350, 500, 700, 1000, 1300, 1700, 2300, 3000 and 4000 metres below the sea surface. Vertical movement of the mesh is handled with an ALE formulation, as is described in Delandmeter et al. (2018).

2.2.4. Initial conditions and forcings

The system is initially at rest with zero elevation and velocity. The salinity is set to $S = 35 \times 10^{-3}$ in the ocean and $S = 0$ in the river. The initial temperature is a piecewise linear function of depth, with a surface temperature of 25°C, decreasing to a minimum value of 8°C in the deeper parts of the domain ($h > 500$ m). For the latter, since global products such as Mercator or HYCOM are not available before 1993, we construct a stratified field similar to that of Denamiel et al. (2013).

The river discharge is imposed at Matadi, the upstream boundary of the domain, based on volumetric flow rate measurements made at the Inga dam, located about 30 km upstream of Matadi. As can be seen in Fig. 3, the period sampled by Eisma (1990) is marked by a relatively low river outflow (about 4.5×10^4 m^3/s) in comparison to climatological values for December (about 5.6×10^4 m^3/s). Only freshwater enters the domain at Matadi and the temperature is set to a constant value of 27°C. While there are several rivers along the African coast inside the computational domain, like the Nyanga and Kwanza Rivers, the Congo River is the only freshwater input taken into account in the model as its volumetric flow rate is about two orders of magnitude greater than the other rivers.

At the open ocean boundaries, tidal elevation and current from OSU TOPEX/Poseidon Global Inverse Solution TPXO7.2 dataset (Egbert and Erofeeva, 2002) are prescribed. No global ocean circulation is prescribed at the open boundaries. The wind stress is generally small in the region of interest (Denamiel et al., 2013). We impose the air–sea flux of momentum with the reanalysis product of ECMWF for the wind

speed at 10 m above sea level. The air–sea heat-flux is not taken into account. As will be seen later, the renewing time of surface waters is quite small, hence limiting the impact of heat fluxes on the estuarine hydrodynamics. The influence of waves in the estuary is also quite limited because of the large river outflow and the topography of the mouth, with the beach barriers almost disconnecting the estuary from the open ocean. The estimated net atmospheric water flux over the area of the estuary is insignificant as compared to the river inflow.

2.3. Renewing water age

Inspecting fields of primitive variables (velocity, pressure, density, etc.) is not necessarily the best approach to the understanding of transport processes taking place over timescales longer than those related to tides (i.e. subtidal timescales). As pointed out above, evaluating time- and position-dependent diagnostic timescales may be conducive to useful interpretations. This is mainly because such timescales lead to an integrative, holistic view of transport phenomena, which is much less affected by small time and space scales of variation than primitive variables (see, e.g., the review article by Lucas and Deleersnijder (2020)).

In this context, inspiration is sought in the generic approach to water renewal developed by Gourgue et al. (2007). Accordingly, the water is split into several water types, namely the water particles present in the control domain at the initial time, the original water, and those progressively replacing them, which belong to the renewing water and originate from open boundaries. The renewing water may be further divided into two components according to whether they come from the upstream boundary (river water or, equivalently, freshwater) or the downstream one (coastal ocean water). At a given time and location, the age of the renewing water or one of its components is the
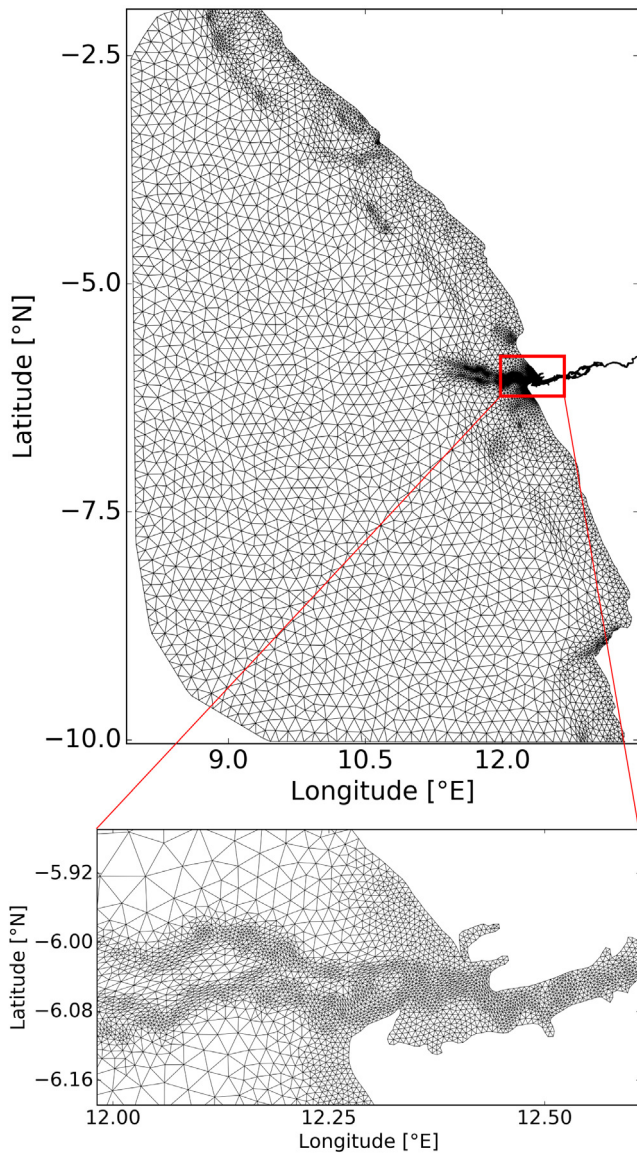
Fig. 4. Top view of the horizontally-anisotropic mesh of the Congo River and adjacent coastal ocean. The mesh resolution ranges from 300 m to 10 km. It has about 1.6×10^4 surface elements. The resolution of the canyon sides is improved by using anisotropic elements (Legrand et al., 2007). This mesh is further extruded in the vertical direction to form columns of prismatic elements with a vertical resolution ranging from 1 to 800 m.

time elapsed since leaving the relevant open boundary (Rayson et al., 2016; Liu et al., 2017; Du et al., 2018; Rutherford and Fennel, 2018). Such ages allow gaining insight into water renewal rates (de Brye et al., 2012; Kärnä and Baptista, 2016b; Yang et al., 2019). In the present study, these diagnoses will help clarify the effects of the estuarine circulation on the long-term transport and the emergence of hypoxia and anoxia in the estuary.

The aforementioned ages are evaluated in accordance with the Constituent-oriented Age and Residence time Theory (CART, www.climate.be/cart) (Delhez et al., 1999; Deleersnijder et al., 2001) Let t and x denote the time and the position-vector, respectively. Then, subscripts *ori*, *riv* and *oce* are introduced so as to identify original, river and oceanic waters. Since it has long been acknowledged that a water type may be regarded as a passive tracer (Cox, 1989; Hirst, 1999; Goosse et al., 2001; Deleersnijder et al., 2002; Haine and Hall, 2002; Meier, 2005; de Brye et al., 2012), the concentration of a water type $C_\chi(t, x)$ obeys advection–diffusion equation

Table 1
Initial and boundary conditions used to solve concentration and age concentration equations (Eqs (1) and (2), from which water type ages are obtained.

Initial condition	Boundary conditions		
$t = 0$	Γ^{riv}	Γ^{oce}	Γ^{imp}
$C_{ori} = 1$	$C_{ori} = 0$	$C_{ori} = 0$	No flux
$C_{riv} = 0$	$C_{riv} = 1$	$C_{riv} = 0$	No flux
$C_{oce} = 0$	$C_{oce} = 0$	$C_{oce} = 1$	No flux
$\alpha_{ori} = 0$	$\alpha_{ori} = 0$	$\alpha_{ori} = 0$	No flux
$\alpha_{riv} = 0$	$\alpha_{riv} = 0$	$\alpha_{riv} = 0$	No flux
$\alpha_{oce} = 0$	$\alpha_{oce} = 0$	$\alpha_{oce} = 0$	No flux

$$\frac{\partial C_\chi}{\partial t} = -\nabla_h \cdot \left(C_\chi \boldsymbol{v} - \boldsymbol{K} \cdot \nabla_h C_\chi \right), \qquad \chi = ori, riv, oce, \quad (1)$$

where $\boldsymbol{v}(t, x)$ is the water velocity, which is divergence-free (Boussinesq approximation), and $\boldsymbol{K}(t, x)$ is the diffusivity tensor. The latter is symmetric and positive-definite. Its components are the same as in the temperature and salinity equations. The age of every water type is $a_\chi = \frac{\alpha_\chi}{C_\chi}$, where age concentration α_χ is the solution of

$$\frac{\partial \alpha_\chi}{\partial t} = C_\chi - \nabla_h \cdot \left(\alpha_\chi \boldsymbol{v} - \boldsymbol{K} \cdot \nabla_h \alpha_\chi \right), \qquad \chi = ori, riv, oce. \quad (2)$$

The first term on the right-hand side of Eq. (2) is related to ageing: the age of every water type particle increases at the same pace as time.

Key ingredients for the evaluation of the ages are the definition of the control domain as well as the initial and boundary conditions under which Eqs. (1) and (2) are to be solved (Deleersnijder et al., 2020). They must be in line with the declared objectives of the diagnostic strategy, which consists in diagnosing water renewal in the river and the adjacent coastal zone. Therefore, the control domain is to be smaller than, and included in, the computational one. The control domain's (open) upstream boundary (Γ^{riv}) coincides with the riverine boundary of the computational domain, which is located at Matadi. Strictly speaking, the estuary begins just upstream of Malela (Spencer et al., 2013). The impact of setting the upstream boundary at Matadi will be discussed in Section 3.4. The (open) oceanic boundary (Γ^{oce}) is relatively close to the coastline: it is located at the mouth of the river and links Pointe de Bulambemba (DRC) in the North and Punta do Padrao (Angola) in the South (red line in the lower right panel of Fig. 1). The remainder of the boundary, including the water–air interface, is impermeable and is denoted Γ^{imp}.

The initial and boundary conditions are laid out in Table 1 and are illustrated in Fig. 5. A zero flux boundary condition is imposed at the impermeable boundaries (Γ^{imp}), and Dirichlet boundary conditions are imposed at other boundaries. While the open boundary conditions for the age concentration are simply $\alpha_\chi = 0$, the open boundary conditions for the water mass concentration depend on whether the inflow brings the water mass of interest ($C_\chi = 1$) or not ($C_\chi = 0$).

Deleersnijder (2019) demonstrated that, as expected, the water concentrations satisfy inequalities $0 \le C_\chi(t, x) \le 1$. In addition, the sum of the concentrations under consideration, i.e. the water concentration, is equal to unity at any time and location ($C_{ori} + C_{riv} + C_{oce} = 1$). It can also be seen that the L^2-norm of the original water concentration monotonically decreases as time progresses so that $C_{ori}(\infty, x) = 0$. In other words, in the long run, the original water is replaced by riverine and oceanic waters, which eventually fill the whole domain, i.e. $C_{riv}(\infty, x) + C_{oce}(\infty, x) = 1$. The riverine and oceanic water ages can be seen to be positive and smaller than the elapsed time, which is the least we can expect from such diagnostic timescales. The age of the original water is equal to the elapsed time, $a_{ori}(t, x) = t$. Obviously, this result provides no insight into water renewal processes, but is a validation element of the present diagnostic strategy. Finally, in accordance with the age-averaging hypothesis formulated by Deleersnijder et al. (2001), we can also aggregate the riverine and oceanic waters, yielding the renewing water, hereinafter identified by subscript *ren*. Its concentration, age concentration and age are $C_{ren} = C_{riv} + C_{oce}$, $\alpha_{ren} = \alpha_{riv} + \alpha_{oce}$ and $a_{ren} = \frac{\alpha_{ren}}{C_{ren}}$, respectively.
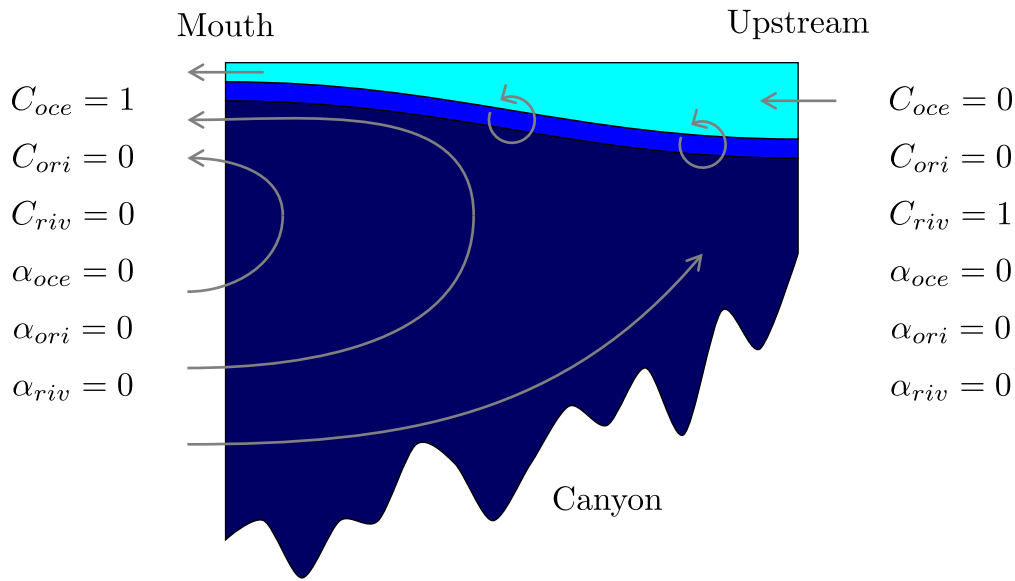
Fig. 5. Sketch of the vertical circulation in the canyon of the Congo River from the mouth to the upstream end of the canyon. Boundary conditions for the renewing water age equations are detailed. C_χ and α_χ are the concentration and the age concentration of χ, respectively. Subscripts *oce*, *ori* and *riv* stand for oceanic, original and riverine water, respectively. Grey arrows represent the subtidal transport of water.
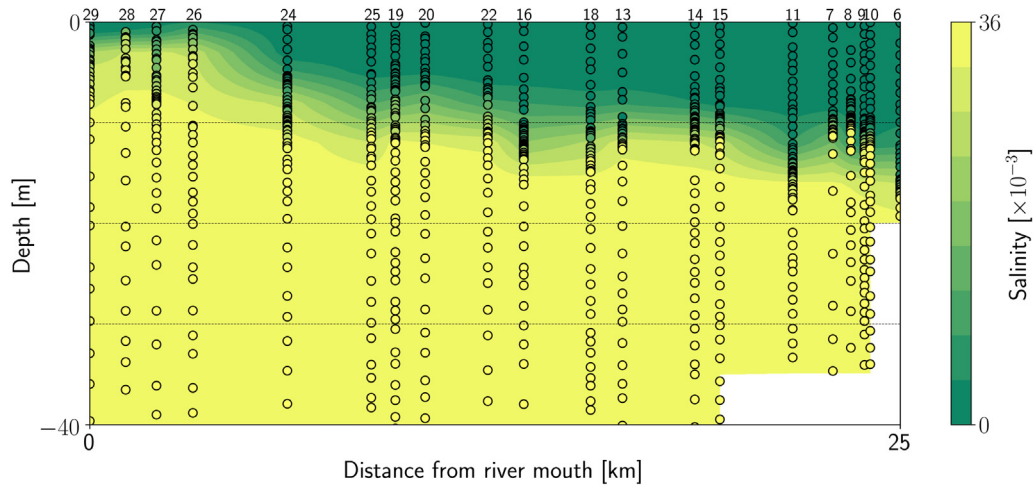

Fig. 6. Comparison of simulated salinity (transect view) in the canyon with field data (filled dots). Numbers above observations indicate the station number for reference to Table A.3.

3. Results

Model results are first compared with the observations collected by Eisma (1990) in December 1989. We then discuss the position of the Congo River estuary within the estuarine classification of Geyer and MacCready (2014) and highlight the two-layer flow structure. We also compute the renewing water age and use it to gain insight into the water renewal timescales of the estuary. We finally sketch an oxygen budget for the estuary.

3.1. Comparison with field data

The model results are compared with the observed salinity and temperature vertical profiles. Model outputs are sampled at the same time stamps as the observations. We then merge simulated vertical profiles in a transect view (Figs. 6 and 7). The simulated halocline is similar to the observed one, with a freshwater layer thickness ranging from about 15 m at the upstream station, to about 5 m at the river mouth (Fig. 6). The strong stratification observed in situ is well captured by the model,

with a thickness of the brackish water layer of a few metres. The sharp transition between water masses shown in the temperature field is also well captured by the model (Fig. 7). In deeper areas, the temperature is somewhat overestimated. The vertical profiles are nonetheless very similar, and vertical gradients of temperature agree between observed and simulated values. The temperature bias is likely due to the ocean initial and boundary conditions, which might be slightly too warm.

Skill metrics are computed to assess the quality of the simulated temperature and salinity fields (see Tables A.3 and A.4). Correlations between observations and predicted values are high at all stations for the salinity (>0.87) and the temperature (>0.92). Small biases are found in the salinity field, because salinity differences in the ocean are small as compared to the temperature differences. The predicted salinity values show less variability than in the observations, with very small (normalised) root mean square errors (RMSE and NMSE).

There is very little information to validate the velocity field in the estuary. Let us just point out that Eisma (1990) reported a velocity of about 2 m/s, just upstream of Malela, at the head of the canyon. The model simulates a velocity of about 1.5 m/s at that location. It
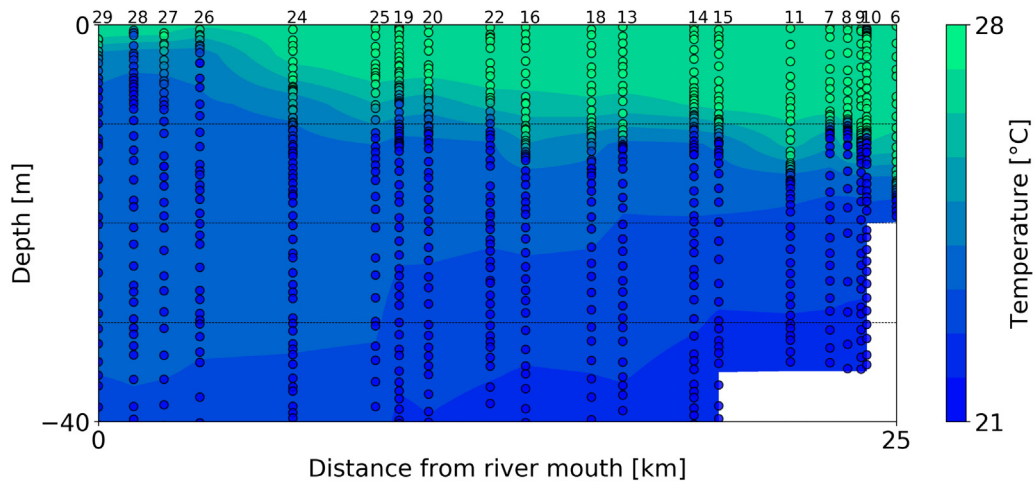
Fig. 7. Comparison of simulated temperature (transect view) in the canyon with field data (filled dots). Numbers above observations indicate the station number for reference to Table A.4.
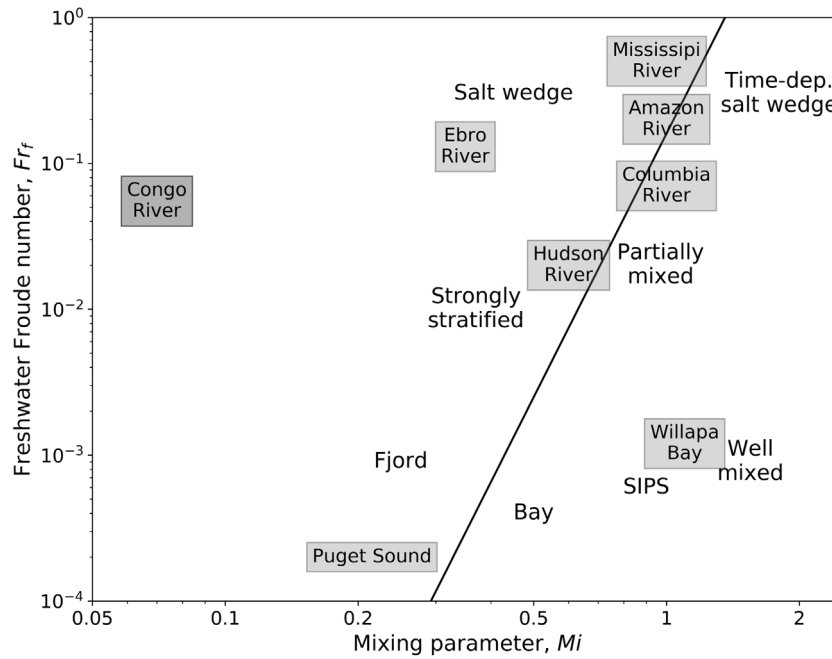

Fig. 8. The estuarine parameter space adapted from Geyer and MacCready (2014). The Congo River (dark grey) appears in the upper (high freshwater Froude number) left (low mixing) corner, underscoring its strongly stratified nature. The line represents the theoretical separation between permanently stratified estuaries and those being possibly vertically mixed.

is noteworthy that the velocity in this region strongly depends on the bathymetry, which is not well documented outside of the canyon. At the bottom of the canyon, Shepard and Emery (1973) reported current velocities up to 0.16 m/s in the up-canyon direction and less intense (up to 0.11 m/s) in the down-canyon direction. To compensate for the outflow of saltwater near the surface, the time-average was reported to be up-canyon, which is also simulated with the model (Fig. 9). Down-canyon strong turbidity currents may abruptly reverse this net upward flow but those cannot be simulated by the present model.

3.2. Estuarine classification

In order to better understand the hydrodynamic regime of the Congo River estuary, we attempt to position it in the Geyer and MacCready (2014) diagram, which is based on the freshwater Froude (Fr_f) and

mixing (Mi) dimensionless numbers (Fig. 8). The freshwater Froude number compares the river flow velocity to the speed of internal waves:

$$Fr_f = \frac{U_R}{\sqrt{\beta g S_o H}}, \tag{3}$$

where $U_R = Q/A$ is the sectionally and tidally averaged river flow velocity, $\beta = 7.7 \times 10^{-1}$ is the haline contraction coefficient, $S_o = 35 \times 10^{-3}$ is the maximal ocean salinity at the river mouth, $H = A/W$ is the characteristic depth of the estuary. For a section of the Congo estuary of area $A \approx 2 \times 10^5$ m^2 and width $W \approx 4 \times 10^3$ m (similar to that of the red dot in the inset of Fig. 1), we obtain $U_R \approx 0.2$ m/s and $H \approx 50$ m. The resulting freshwater Froude number value, $Fr_f \approx 5.5 \times 10^{-2}$, is comparable to that of other high-discharge rivers such as the Columbia River (Kärnä and Baptista, 2016a).
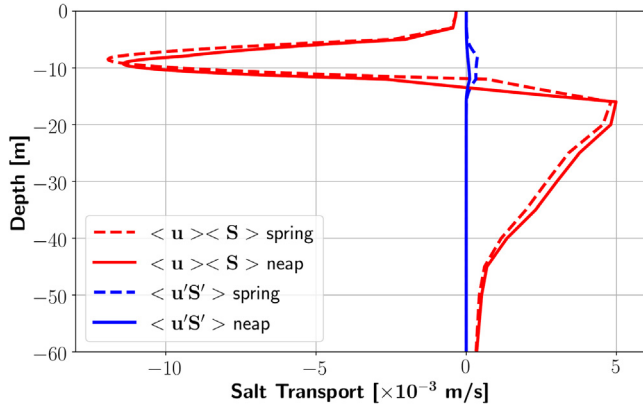
Fig. 9. Salinity transport in the Congo River estuary at the station represented by a red dot in Fig. 1. The signal is largely dominated by the mean components (red). Mean tidal transport (blue), localised in the brackish waters, is larger during spring tides (dashed) than during neap tides (solid) but remains one order of magnitude smaller. The characteristic two-layer dynamics of strongly stratified estuaries is very clear.

The mixing number evaluates the effectiveness of tidal mixing for a stratified estuary:

$$Mi = \sqrt{\frac{u_*^2}{\omega N_0 H^2}}, \qquad (4)$$

where $u_*^2 = C_D U_T^2$ is the bottom stress, $\omega = 1.4 \times 10^{-4}$ s^{-1} is the dominant (M$_2$) tidal frequency in the Congo River estuary, and $N_0 = \sqrt{\frac{\beta g S_o}{H}} \approx 7.3 \times 10^{-2}$ s^{-1} is the buoyancy frequency. With an amplitude of the depth-averaged tidal velocity $U_T \approx 0.2$ m/s and $C_D = 3 \times 10^{-3}$, the squared friction velocity is $u_*^2 \approx 10^{-4}$ m^2/s^2, which is comparable to values computed by means of the hydrodynamic model. The resulting mixing parameter value $Mi \approx 7 \times 10^{-2}$ is very small and comparable to that of fjords. This is due to the combined effect of a small tidal amplitude signal in this region and the canyon's depth, comparable to that of a fjord. Unlike classical fjords, the freshwater Froude number is rather large despite the depth of the canyon. This is a consequence of the very large river discharge. The Congo River estuary thus appears as an outlier in the Geyer and MacCready (2014) estuarine parameter space (Fig. 8).

3.3. Two-layer flow structure

The Congo River estuary exhibits a very stable stratification as the tides are not strong enough to erode the pycnocline. In order to quantify the comparative effects of the tidal and gravitational circulations, we compute the different components of the residual salinity transport, $\langle uS \rangle$, using the vertical profiles of the along-channel velocity, $u = u(z,t)$, and salinity, $S = S(z,t)$, at a station inside the estuary (red dot in Fig. 1). The total salt transport $\langle uS \rangle$ can be expressed as

$$\langle uS \rangle = \langle u \rangle \langle S \rangle + \langle u'S' \rangle, \qquad (5)$$

where f' represents the deviation from the tidal average $\langle f \rangle$. This splitting allows us to evaluate the transport due to the exchange flow, as compared to the dispersive tidal salt transport (Hamilton, 1990). The first term on the right hand side of Eq. (5) represents the advection of the mean salinity profile by the residual velocity field. The second term represents the transport due to tides.

The typical two-layer structure of the exchange flow is clearly visible in the transport profiles (Fig. 9). The temporal average is computed over four tidal periods in both spring (dashed curves) and neap (solid curves) tidal phases (see Fig. 3 for the time periods). The mean value (red curves) shows that there is a large net seaward transport in the top layer, as explained by Spencer et al. (2013). Below it, the net salt flux is landward, which is typical of strongly stratified estuaries and fjords. The transition between the two distinct layers is very sharp but, unlike shallow rivers where maximum inflow is near the bottom, the landward component is mainly restricted to the top 40 m. It is not significant at larger depths, appearing more like the circulation in a fjord, with a third layer in which the current is slower. The tidal effects (blue curve) have an almost negligible influence on the total transport, as in fjords and strongly stratified estuaries. The tidal transport is restricted to the pycnocline area. Overall, the flow is mostly baroclinic and gravitational effects dominate the tidal effects.

The variability of the velocity over a tidal period is shown in Fig. 10, where the two-layer structure of the flow clearly appears. In the bottom layer, the flood tide increases the landward current, but ebbing tides barely change the velocity direction there. The top layer seaward velocity also exhibits small tidal variability, with small changes of the seaward velocity.

Geyer and Ralston (2011) examined the dynamics of strongly stratified estuaries using the two-layer theory. They split those into two
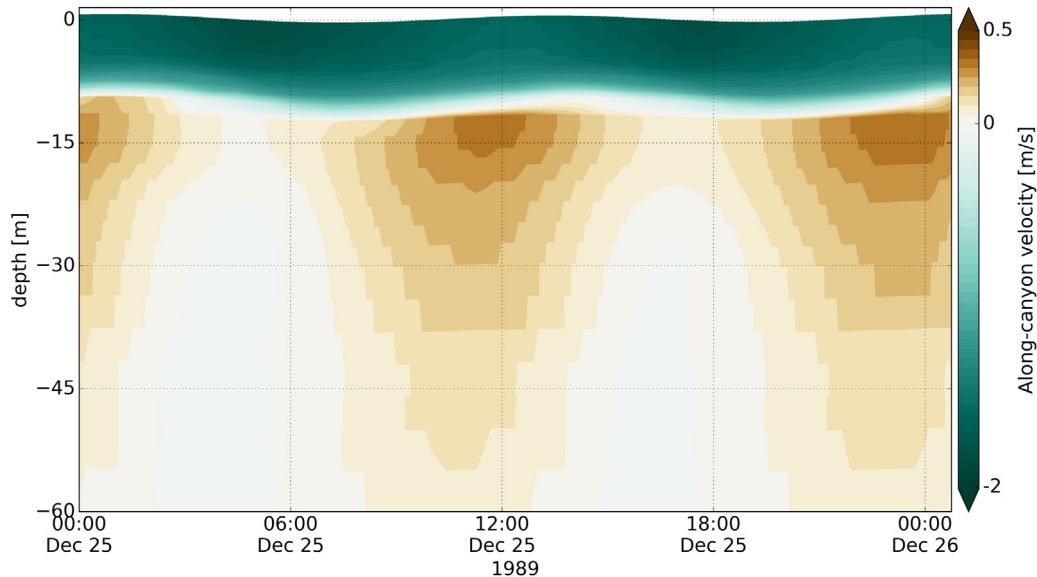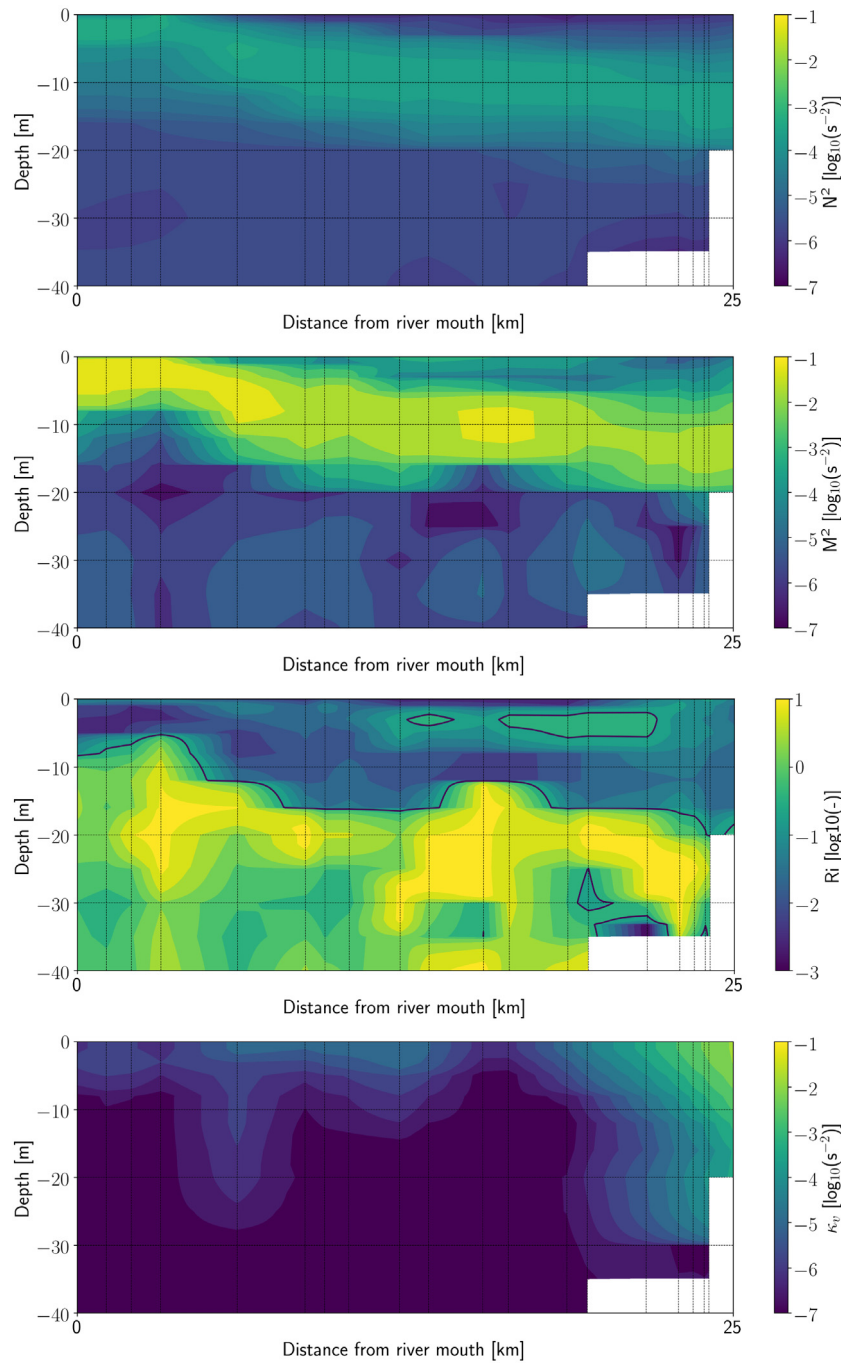

Fig. 10. Velocity profile evolution over two tidal periods at the station represented by a red dot in Fig. 1. The two-layer structure of the flow exhibits small tidal variability, although the magnitude varies. Positive values mean the current is pointing towards the upstream boundary.

Fig. 11. Vertical along-canyon transect of the squared buoyancy frequency N^2, squared shear frequency M^2, gradient Richardson number $Ri = \frac{N^2}{M^2}$ and vertical turbulent diffusivity κ_v in the Congo River estuary. All values are averaged over several days, and are representative for both spring and neap tides. The x-axis is the distance from the mouth towards the upstream river. The solid lines on the third panel represent the steady-state isolines $Ri = 0.25$. Vertical mixing is very small in deep areas, where vertical diffusivity and stratification are small. It only becomes significant in the upstream shallow regions. Note the logarithmic scale for all variables.

categories: salt wedge and fjord. The former is characterised by a discharge sufficiently large to recover strong stratification despite tides and comparable thickness between top and bottom layers. The stratification in the latter arises from the decorrelation between surface and bottom layer dynamics. The depth of fjords is quite large, and the top layer is often very thin as compared to the bottom layer. Tides also have a limited impact on the surface layer dynamics. The Congo therefore shares many similarities with fjords, despite its huge river discharge.

The turbulent kinetic energy, which increases with shear and decreases with stratification, controls the vertical mixing. The dynamic stability of the water column can thus be investigated with the gradient Richardson number, $Ri = \frac{N^2}{M^2}$. The latter is the ratio of the following parameters: the squared Brunt–Väisälä (buoyancy) frequency $N^2 = -\frac{g}{\rho_0}\frac{\partial\rho}{\partial z}$ and the squared shear frequency $M^2 = \|\frac{\partial u}{\partial z}\|^2$. Fig. 11 shows profiles of those parameters along the canyon transect. As expected, both frequencies are higher along the pycnocline where the stratification is strongest. As the shear frequency is smaller than the buoyancy frequency in deep areas, the gradient Richardson number is large in many places, except near the pycnocline and the sea surface. The resulting vertical turbulent diffusivity is therefore very small throughout the deep water column. It mainly becomes significant in shallower regions, at the head of the canyon.
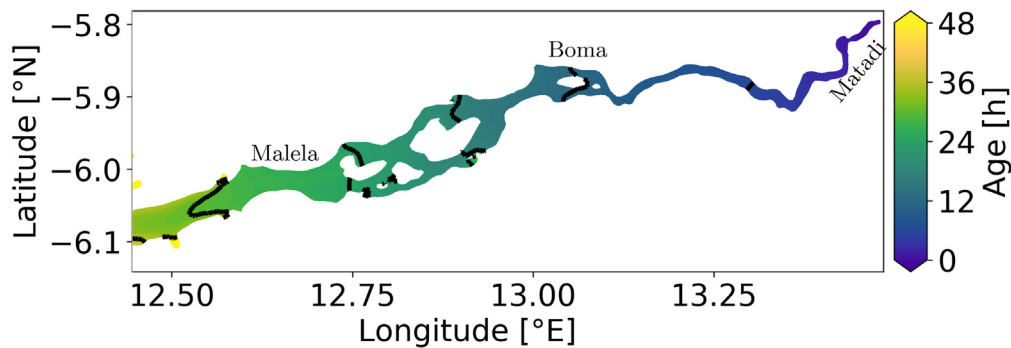
Fig. 12. Surface renewing water age in the Congo River. The scale is in hours and the thick black lines show every 6 h interval.

3.4. Renewing water age

We study the renewing of the estuarine water and differentiate water masses originating from the ocean and the river. Renewing water age is simulated for the same time period as the hydrodynamics.

The surface renewing water age is shown in Fig. 12. The riverine waters rapidly flows out of the river when leaving Matadi, reaching Boma in about 12 hours and Malela in about 1 day. They eventually enter the ocean after about 1.5 days. Upstream of the canyon, there is little variability of the surface freshwater age across the channel. However, over the canyon, bottom friction is reduced and, combined with the gravitational current, surface waters tend to accelerate. As a result, lateral variability grows with a smaller age over the canyon and larger values in the vicinity of the river banks, leading to a parabolic-like age profile.

As the water column is well-mixed in the upstream part of the river, age estimates are in good agreement with the barotropic estimates of Le Bars et al. (2016). The depth-averaged renewing water age near Boma was estimated to be less than one day with the 2D model, whereas surface water age computed with the 3D model is about 12 hours. Density-driven currents tend to accelerate surface waters, leading to smaller ages. In the estuary, estimates vary more significantly. The barotropic model showed a strong deceleration near the mouth, with a transition of river water age from 2 days at Malela to more than 10 days at Banana. In the 3D model, the water age shows that water accelerates at the surface, reaching the river mouth in less than 1.5 days. Of course, the oceanic water age sharply increases in the bottom layer and hence partly compensates these differences. However, in the estuary, the 3D baroclinic model clearly provides a better picture of the water age as there is a strong vertical variability over the water column.

Over the water column, the riverine waters are mainly present in the top layers with a riverine water concentration $C_{riv} > 0.99$ in the top 5 m of the water column of the estuary and $C_{riv} < 0.01$ below 15 m (not shown). The oceanic waters slowly fill the bottom layer. In between, brackish waters result from the mixing of those two water masses.

The renewing water age in the top 15 metres is shown in Fig. 13 (top panel). Near the pycnocline, the structure is similar to that observed in other stratified estuaries (Kärnä and Baptista, 2016b). The renewing water age is small ($a < 2$ days) in this top layer where freshwater is mostly present ($C_{riv} \gg C_{oce}$). The age is also small near the open ocean boundary just below the pycnocline (> 8 m), where oceanic waters are mostly present ($C_{oce} \gg C_{riv}$). Between those two layers, brackish waters are trapped by the strong mixing and the renewing water age increases ($a > 3$ days). It is noteworthy that the riverine water age is computed since leaving Matadi, while the Congo River estuary is defined as starting just upstream of Malela. The time spent by the riverine water inside the estuary itself is thus smaller, by approximatively 1 day.

Yet, this aforementioned local age maximum is not the global maximal value over the water column. As the maximum salinity inflow is located far from the bottom in the case of the Congo due the

significant depth of the estuary, there is an inflow of older water in deeper areas where shear stress (and hence mixing) is reduced. Near the bottom of the canyon, there is therefore no trace of riverine water. The renewing water age coincides with the oceanic water age and grows with depth (Fig. 13, bottom panel). It exceeds two months at some places. The dense oceanic water masses with a low dissolved oxygen concentration enter with the gravitational circulation and stagnate in the deep estuary, like in a fjord. These water masses do not mix with the lighter riverine water masses. The long renewal time during which waters originating from the Eastern Equatorial oxygen minimum zone enter the deeper parts of the canyon, combined with the degradation of riverine organic material, presumably cause the formation of areas with very low oxygen concentrations. The locations of the renewing water age maxima seem to correspond with the observed oxygen minima.
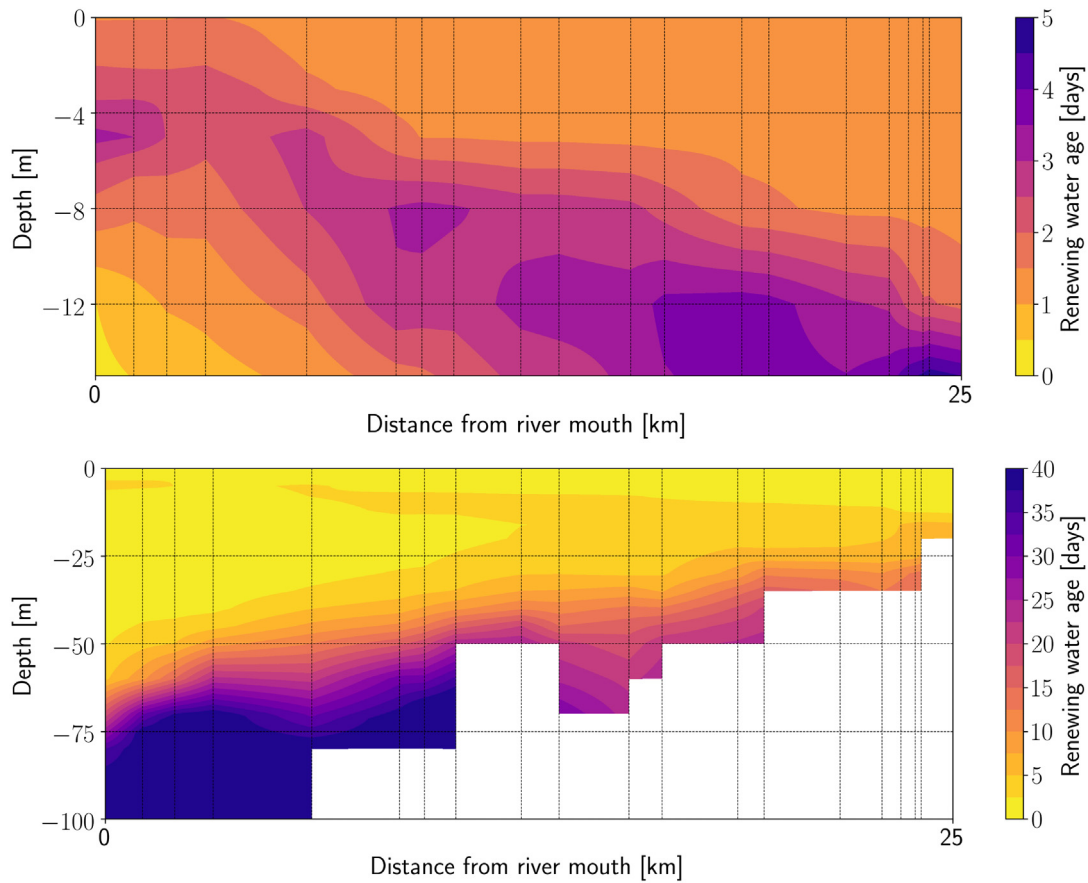
The head of the canyon is characterised by an abrupt halt of the oceanic water intrusion (not shown). At Malela, there is an abrupt transition between the outer (deep) and the inner (shallow) parts of the estuary (Dupra et al., 2001). With the steep transition to shallow areas and the large river discharge, the oceanic waters are blocked. Only riverine freshwater fills the inner estuary. The salinity intrusion length is therefore very stable over time.
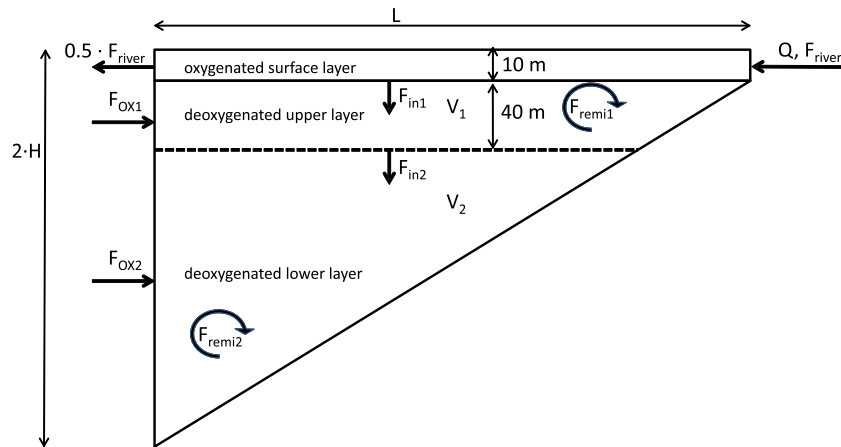
3.5. Schematic oxygen budget

Oxygen in the estuarine canyon below the freshwater layer is increasingly depleted with depth, reaching almost zero near the bottom (Fig. 2). This is due to: (i) aerobic respiration of particulate organic carbon (POC) that is flushed from the upstream Congo River and gravitationally settles into the deeper layers once it arrives at the estuary, (ii) strong density stratification restricting vertical mixing of atmospheric oxygen into deeper layers and (iii) advection of oxygen depleted oceanic waters into the estuarine canyon.

Here, we estimate the role of POC-remineralisation for the estuarine canyon's oxygen and carbon balance with a 3-box model in a simplified geometry (Fig. 14), where a shallow oxygenated upper layer of constant depth (10 m) lies on top of a deoxygenated lower layer, whose depth increases with the distance to the upstream boundary. From the vertical structure of oxygen measurements (Fig. 2) and simulated ocean water renewal times (Fig. 13), the deoxygenated area can be subdivided into an upper and a lower zone. The upper deoxygenated zone is characterised by a relatively fast exchange of water with the upper ocean and a strong input of POC. The lower anoxic zone exchanges more slowly with the corresponding deep ocean water. POC which is not remineralised within the upper canyon reaches this zone and its labile fraction can be partly remineralised there, with provision of less oxygen. Both deoxygenated zones are separated at 50 m depth. The volume of the estuarine canyon is 10^{10} m^3, from approximate length scales width $W = 2$ km, length $L = 25$ km and mean depth $H = 200$ m.

The upper and lower deoxygenated zones' water renewal times are $R_1 = 5.4$ days and $R_2 = 47.7$ days, respectively. They are calculated as

Fig. 13. Renewing water age in the Congo River canyon. (a) Young waters go through the whole estuary in the top fresh layer. Brackish waters are trapped below this top layer and, hence, tend to become older. (b) The age in the bottom of the estuary is much larger than the age at the surface. Dense waters become older as they are slowly moving inland due to the exchange flow. The colormap is limited to 40 days for clarity, the maximal value reaches 60 days.

Fig. 14. Sketch of the geometry and the fluxes relevant for the oxygen and carbon budget along a longitudinal section of the canyon. The different terms are defined in Table 2.

volume weighted averages of the simulated high resolution water age distribution.

The oxygen concentrations of the upper ($[O_2]_1 = 0.189$ mol m^{-3}) and lower ($[O_2]_2 = 0.085$ mol m^{-3}) oceanic renewal waters are calculated as vertical averages from an oxygen profile at a station 121 km downstream of the upper end of the estuary (Eisma, 1990). The lower oceanic waters originate in the Eastern Equatorial oxygen minimum zone (Karstensen et al., 2008).

The oxygen budget in the upper deoxygenated layer is given by the net influx of O$_2$ (F_{ox1}) from the inflowing oceanic waters during the renewal time (R_1) and by the concurrent loss of oxygen due to

remineralisation of labile POC settling from surface oxygenated layer. The POC remineralisation rate (F_{remi1}) is equivalent to the oxygen consumption, as the stoichiometric ratio of oxygen (O$_2$) consumption to organic carbon (labile POC) consumption is 1 (Paulmier et al., 2009). Pelagic remineralisation is computed as the difference between oxygen advected with ocean water and oxygen observed *in situ*. Exchange of oxygen with the surface layer is not taken into account because it is largely prevented by the halocline. For the lower deoxygenated layer we assume the corresponding fluxes.

The carbon budget in the upper deoxygenated layer is given by the amount of labile POC settling from the oxygenated layer (F_{in1}) and its

Table 2

Summary of the fluxes and other quantities shown in Fig. 14.

Q	Congo River discharge (Coynel et al., 2005)	37047	$\text{m}^3\,\text{s}^{-1}$
[POC]	POC concentration at canyon head	0.092	mol C m^{-3}
F_{river}	POC flux from Congo River ($= Q \cdot$ [POC])	3408	mol C s^{-1}
σ	Fraction of F_{river} settling out of the oxygenated surface layer	0.5	–
λ	Fraction of POC labile to remineralisation	0.3	–
F_{in1}	Influx of labile POC into the upper deoxygenated zone ($= F_{\text{river}} \cdot \sigma \cdot \lambda$)	551.2	mol C s^{-1}
F_{in2}	Influx of labile POC into the lower deoxygenated zone ($= F_{\text{in1}} - F_{\text{remi1}}$)	283.7	mol C s^{-1}
F_{ox1}	Influx O_2 from upper ocean ($= [O_2]_1 \cdot \frac{V_1}{R_1}$)	779.0	$\text{mol O}_2\,\text{s}^{-1}$
F_{ox2}	Influx O_2 from lower ocean ($= [O_2]_2 \cdot \frac{V_2}{R_2}$)	166.6	$\text{mol O}_2\,\text{s}^{-1}$
F_{remi1}	Pelagic remineralisation (upper) ($= ([O_2]_1 - [O_2]_{\text{up}}) \cdot \frac{V_1}{R_1}$)	270.0	mol C s^{-1}
F_{remi2}	Pelagic remineralisation (lower) ($= ([O_2]_2 - [O_2]_{\text{lo}}) \cdot \frac{V_2}{R_2}$)	70.4	mol C s^{-1}
R_1	Mean water renewal time (upper)	5.4	days
R_2	Mean water renewal time (lower)	47.7	days
R	Mean water renewal time (total box)	27.3	days
L	Length of the canyon	25000	m
W	Width of the canyon	2000	m
H	Mean depth	200	m
V	Volume of the entire canyon (0–400 m)	10^{10}	m^3
V_1	Volume of the upper canyon (10–50 m)	$1.92 \cdot 10^9$	m^3
V_2	Volume of the lower canyon (50–400 m)	$8.03 \cdot 10^9$	m^3
red	Ratio of oxygen to carbon consumption	1	$\text{mol O}_2/\text{mol C}$
$[O_2]_{\text{up}}$	Oxygen concentration canyon (upper)	0.123	$\text{mol O}_2\,\text{m}^{-3}$
$[O_2]_{\text{lo}}$	Oxygen concentration canyon (lower)	0.049	$\text{mol O}_2\,\text{m}^{-3}$
$[O_2]_1$	Oxygen concentration ocean (upper)	0.189	$\text{mol O}_2\,\text{m}^{-3}$
$[O_2]_2$	Oxygen concentration ocean (lower)	0.085	$\text{mol O}_2\,\text{m}^{-3}$

loss due to remineralisation while settling (F_{remi1}). According to Eisma and Kalf (1984), half of the Congo River's POC flux settles into the deeper part of the estuary, the other half being advected offshore with the surface current. This value of 50% is consistent with the results from a recent study on trace elements originating from the Congo River (Vieira et al., 2020). We therefore take F_{in1} as the labile fraction of $F_{\text{riv}}/2$. The carbon budget in the lower deoxygenated layer is given by the amount of labile POC settling from the upper deoxygenated layer (F_{in2}) and its loss due to remineralisation while settling (F_{remi2}).

The riverine POC flux (F_{riv}), calculated as the product of discharge and POC concentration, deviates from the annual average by less than 2% during the seasonal low and high water periods, according to monthly measurements at a station near Brazzaville/Kinshasa about 300 km upstream of the estuary (Coynel et al., 2005). River suspension apparently becomes diluted with discharge. We assume no change in water discharge from Kinshasa to the river mouth and therefore use the annual average given by Coynel et al. (2005). For the POC concentration, they report an annual average of $1.7\,\text{mg C l}^{-1}$, which is significantly higher than the $1.1\,\text{mg C l}^{-1}$ reported as average by Cadée (1984) for the estuarine freshwater. This indicates a loss of POC due to sedimentation within the river between Kinshasa and the river mouth. We therefore use the POC concentration of $1.1\,\text{mg C l}^{-1}$ (= $0.092\,\text{mol C m}^{-3}$) from Cadée (1984).

Only a fraction of POC is labile, i.e. susceptible to remineralisation. This fraction has been estimated as 22%–46% for rivers with Total Suspended Solids (TSS) < $150\,\text{mg l}^{-1}$ (e.g. 20%–25% for the Ganges, Brahmaputra, Indus and Orinoco rivers) by Ittekott (1988). For the Congo River, we expect values towards the lower end of that range due to the river's comparatively low TSS (annual average $26\,\text{mg l}^{-1}$ (Coynel et al., 2005)), which is predominantly (80%) in the "fine" fraction (<63 microns), with its POC originating from relatively degraded soil organic matter (Spencer et al., 2012).

The carbon and oxygen budget for the subhalocline layer of the canyon critically depends on the ocean water's oxygen concentration and renewal time, the amount of organic matter entering the anaerobic zone and this material's labile fraction. The mean renewal time 27.3 days compares reasonably well with the 20 days-estimate derived from earlier bottom water current measurements of Shepard and Emery (1973) by van Bennekom et al. (1978). Varying the values of renewal times by ±10% results in remineralisation ratios of 60.8–73.5%. This interval includes the standard ratio (with the model based renewal times)

of 67% in narrow limits. Organic matter fluxes are well documented, the labile fraction can be estimated within reasonable limits.

Assuming a labile fraction of 30%, the remineralisation consumes 67% of the labile component of the total settling POC (or 33.5% of the labile component of the total river POC flux) to draw oxygen down to the observed levels in both deoxygenated zones. If the labile fraction were 25% instead, the same oxygen drawdown would result from remineralisation of 80% of the labile component of the total settling POC (or 40% of the labile component of total river POC flux). In other words, a reduction of the Congo's POC flux by more than 33% of its present value (e.g. due to reservoir construction for the "Grand INGA Hydroelectric Project") could initiate re-oxygenation of the subhalocline water body towards aerobic conditions.

4. Discussion and conclusion

Setting up a 3D baroclinic model of the Congo River estuary is very challenging because of the steep bathymetry profile with slopes up to 50% along the submarine canyon. By combining a discontinuous Galerkin formulation, an anisotropic horizontal mesh and σ–z vertical discretisation, we managed to represent both the geometry and the model variables despite these strong gradients. The vertical and horizontal discretisations have to be carefully selected in order to correctly reproduce the circulation within the canyon. Preliminary attempts confirmed that σ layers are not well suited to approximate steep bathymetry profiles. We therefore only used σ layers in the top 12 metres and z layers underneath. The recent implementation of a vertically-adaptive mesh in SLIM 3D (Delandmeter et al., 2018) should also be considered as such a discretisation has proved to be very efficient in previous studies of stratified flows (Burchard and Beckers, 2004; Hofmeister et al., 2010, 2011; Gräwe et al., 2015). The vertical discretisation seems to be more important than the horizontal mesh refinement strategy, although the use of horizontally-anisotropic meshes helps reducing the numerical dissipation by increasing the resolution over the steep slopes of the canyon with a limited computational overhead.

Le Bars et al. (2016) accurately reproduced the tidal propagation in the estuary with a depth-averaged model. Here we have studied the 3D baroclinic dynamics of this system. Some of the results obviously differ between the two studies. Unsurprisingly, gravitational currents play a significant role in the net outflow. The 2D barotropic model estimated that the net outflow varies by about $1.5 \times 10^4\,\text{m}^3/\text{s}$ due to tides.

Table A.3
Skill metrics achieved with SLIM 3D for the salinity at different locations in the canyon. Stations are listed from downstream to upstream, as shown in Fig. 6.

Stations	Bathymetry [m]	Min	Max	Mean	Bias	RMSE	NMSE	Corr
29	454	0.88	35.69	32.46	0.19	0.65	0.05	0.98
28	439	17.64	35.68	33.92	0.43	1.01	0.6	0.98
27	343	2.21	35.8	31.29	0.22	1.54	0.24	0.9
26	315	6.97	35.76	33.44	0.41	0.69	0.11	0.97
24	283	0	35.8	28.51	−0.02	3.28	0.26	0.87
25	215	0	35.8	31.08	0.33	1.35	0.03	0.99
19	209	0.21	35.57	30.05	0.25	1.3	0.03	0.99
20	189	0.1	35.69	30.06	0.16	1.84	0.04	0.98
22	84	0.01	35.67	31.14	0.73	1.16	0.01	1.0
16	164	0.0	35.55	29.59	−0.32	3.29	0.11	0.95
18	139	0.54	35.76	31.67	−0.0	2.95	0.09	0.95
13	181	0	35.47	28.47	−0.06	2.33	0.06	0.97
14	94	0	35.63	26.64	0.85	1.51	0.01	1.0
15	109	0	35.76	29.02	0.83	1.77	0.03	0.99
11	103	0.0	35.51	24.86	−0.52	3.9	0.1	0.95
7	80	0.01	35.53	28.31	2.72	7.01	0.23	0.91
8	103	0.03	35.61	26.03	1.61	5.42	0.27	0.89
9	91	0	35.61	26.82	1.37	3.78	0.08	0.97
10	94	0	35.65	25.26	1.58	4.85	0.14	0.94
6	41	0	35.58	23.33	−2.18	6.3	0.14	0.94

Baroclinic model results suggest a larger variability $> 2.5 \times 10^4$ m^3/s (not shown). It suggests that the outflow may reverse and net inflows towards the river can be expected during dry seasons and flood tides. The gyres that appeared in the 2D model simulations did not appear with the 3D model. Since the sensitivity analysis of Le Bars et al. (2016) showed a strong dependence to the bottom friction parametrisation, a misrepresentation of the bottom velocity (and hence the bottom drag) could have led to unrealistic barotropic features, as depth-averaged velocities are far larger in the 2D model than those predicted near the bottom in the 3D model.

By modelling the renewing water age, we gained insight into the transport timescales of the estuary. This slow renewal can be directly related to the hypoxic and anoxic conditions observed. The exchange flow traps particles such as particulate organic matter or sediments that mix in the pycnocline. These particles flocculate and sink to the bottom waters. Bacteria feed on particulate organic matter and consume oxygen through respiration. Due to the abundant source of particulate organic matter, the number of bacteria grows. Since the water column is highly stratified, there is little vertical mixing and water renewal is hence very limited (Pak et al., 1984). Oxygen is therefore entirely consumed by the respiration of the settling POC.

The peculiar characteristics of the Congo River estuary make it difficult to categorise. As illustrated by Fig. 8, the strongly stratified Congo hydrodynamical regime lies between a very pronounced salt wedge and an unconventionally dynamic fjord. In their theoretical study of highly stratified estuaries, Geyer and Ralston (2011) doubt the existence of any estuary where the salt wedge would not be significantly affected by tides. The Congo is almost contradicting this hypothesis. The microtidal environment and the depth of the canyon allow the stratification to remain strong at all times. This separation between water masses reduces the mixing with oceanic waters in the bottom layer. In the canyon, the dynamics of the Congo River estuary shares more similarities with fjords, such as the decorrelation between the thick bottom layer and the thin surface layer and the high retention of water near the bottom. Even with a very large discharge, the renewing water age exceeds two months at some deep places. The Congo River estuary therefore appears as a hybrid between a strongly stratified estuary and a (hydrodynamic) "fjord in Africa".

CRediT authorship contribution statement

Valentin Vallaeys: Methodology, Software, Validation, Writing – Original Draft, Writing Review & Editing. **Jonathan Lambrechts:** Methodology, Software, Validation, Visualization. **Philippe Delandmeter:** Software, Visualization. **Johannes Pätsch:** Methodology, Validation, Writing - Review & Editing. **Alejandro Spitzy:** Methodology, Writing - Review & Editing. **Emmanuel Hanert:** Conceptualization, Methodology, Validation, Writing - Review & Editing, Supervision. **Eric Deleersnijder:** Conceptualization, Methodology, Validation, Writing Review & Editing, Supervision.

Declaration of competing interest

The authors declare that they have no known competing financial interests or personal relationships that could have appeared to influence the work reported in this paper.

Appendix. Skill metrics

Observed and simulated salinity and temperature fields are compared at different stations using standard metrics: mean bias (Bias), root mean square error (RMSE), normalised root mean square error (NMSE) and Pearson correlation coefficient (Corr). The complete skill metrics are listed in Tables A.3 and A.4. Stations names correspond to the numbers referred to in Eisma (1990) and shown in Fig. 6. Apart from a few exceptions, these numbers follow the path of the river, with smaller numbers corresponding to upstream stations. The metrics prove the ability of the model to represent the hydrodynamics of the estuary. Biases and RMSE are rather small. Correlations are close to 1 at all stations and tables report only small NMSE.

Table A.4
Skill metrics achieved with SLIM 3D for the temperature at different locations in the canyon. Stations are listed from downstream to upstream, as shown in Fig. 6.

Stations	Bathymetry [m]	Min [°C]	Max [°C]	Mean [°C]	Bias [°C]	RMSE [°C]	NMSE	Corr
29	454	9.9	28.29	15.58	−3.16	3.54	0.9	0.94
28	439	10.52	25.05	15.85	−2.91	3.0	0.72	0.98
27	343	10.38	28.59	16.03	−1.61	1.95	0.25	0.98
26	315	10.72	27.32	17.01	−1.76	1.9	0.28	0.99
24	283	12.11	28.71	18.11	−2.42	2.57	0.63	0.96
25	215	13.74	28.83	17.92	−3.08	3.18	1.15	0.97
19	209	14.58	28.93	18.66	−3.66	3.73	1.84	0.97
20	189	13.57	29.04	17.50	−3.24	3.35	1.24	0.97
22	84	14.49	28.99	17.86	−3.48	3.61	1.09	0.99
16	164	15.02	28.58	18.66	−3.7	3.9	1.27	0.96
18	139	14.53	28.54	17.69	−3.75	3.92	1.33	0.97
13	181	14.15	28.59	17.96	−4.31	4.49	1.71	0.95
14	94	15.25	28.82	19.04	−4.36	4.56	1.2	0.99
15	109	14.5	28.82	18.29	−4.75	4.89	1.78	0.99
11	103	15.26	28.39	18.59	−4.56	4.89	1.36	0.96
7	80	15.2	28.84	18.59	−4.68	5.12	1.19	0.93
8	103	15.18	28.88	19.11	−5.26	5.47	2.12	0.94
9	91	15.45	28.92	18.97	−4.85	5.13	1.32	0.98
10	94	15.62	28.98	20.79	−5.04	5.32	1.55	0.96
6	41	15.62	28.49	20.42	−2.39	3.28	0.44	0.92

References

van Bennekom, A., Berger, G., Helder, W., Vries, R.D., 1978. Nutrient distribution in the Zaire estuary and river plume. Netherlands J. Sea Res. 12 (3), 296–323.

Berntsen, J., 2011. A perfectly balanced method for estimating the internal pressure gradients in σ-coordinate ocean models. Ocean Model. 38 (1), 85–95.

Blaise, S., Comblen, R., Legat, V., Remacle, J.-F., Deleersnijder, E., Lambrechts, J., 2010. A discontinuous finite element baroclinic marine model on unstructured prismatic meshes. Part I: Space discretization. Ocean Dyn. 60 (6), 1371–1393.

de Brye, B., de Brauwere, A., Gourgue, O., Delhez, E.J.M., Deleersnijder, E., 2012. Water renewal timescales in the Scheldt Estuary. J. Mar. Syst. 94, 74–86.

Burchard, H., Beckers, J.-M., 2004. Non-uniform adaptive vertical grids in one-dimensional numerical ocean models. Ocean Model. 6 (1), 51–81.

Cadée, G.C., 1984. Particulate and dissolved organic carbon and chlorophyll a in the Zaire river, estuary and plume. Netherlands J. Sea Res. 17 (2), 426–440.

Chao, Y., Farrara, J.D., Schumann, G., Andreadis, K.M., Moller, D., 2015. Sea surface salinity variability in response to the Congo River discharge. Cont. Shelf Res. 99, 35–45.

Cox, M.D., 1989. An idealized model of the World Ocean. Part I: The global-scale water masses. J. Phys. Oceanogr. 19 (11), 1730–1752.

Coynel, A., Seyler, P., Etcheber, H., Meybeck, M., Orange, D., 2005. Spatial and seasonal dynamics of total suspended sediment and organic carbon species in the Congo River. Glob. Biogeochem. Cycles 19 (4).

Delandmeter, P., Lambrechts, J., Legat, V., Vallaeys, V., Naithani, J., Thiery, W., Remacle, J.-F., Deleersnijder, E., 2018. A fully consistent and conservative vertically adaptive coordinate system for SLIM 3D v0.4 with an application to the thermocline oscillations of Lake Tanganyika. Geosci. Model Dev. 11 (3), 1161–1179.

Delandmeter, P., Lewis, S.E., Lambrechts, J., Deleersnijder, E., Legat, V., Wolanski, E., 2015. The transport and fate of riverine fine sediment exported to a semi-open system. Estuar. Coast. Shelf Sci. 167, 336–346.

Deleersnijder, E., 2015. On the pressure gradient error in the sigma-coordinate system, Working Note. Université catholique de Louvain, Louvain-la-Neuve, Belgium, 5 pages. available on the web at http://hdl.h{and}le.net/2078.1/155107.

Deleersnijder, E., 2019. Water renewal of a region of freshwater influence (ROFI): mathematical properties of some of the relevant diagnostic variables, Working Note. Université catholique de Louvain, Louvain-la-Neuve, Belgium, 19 pages. available on the web at http://hdl.h{and}le.net/2078.1/220841.

Deleersnijder, E., Beckers, J.-M., 1992. On the use of the σ-coordinate system in regions of large bathymetric variations. J. Mar. Syst. 3 (4–5), 381–390.

Deleersnijder, E., Campin, J.-M., Delhez, E.J.M., 2001. The concept of age in marine modelling: I. Theory and preliminary model results. J. Mar. Syst. 28 (3–4), 229–267.

Deleersnijder, E., Draoui, I., Lambrechts, J., Legat, V., Mouchet, A., 2020. Consistent boundary conditions for age calculations. Water 12 (5), 1274.

Deleersnijder, E., Mouchet, A., Delhez, E.J.M., Beckers, J.-M., 2002. Transient behaviour of water ages in the World Ocean. Math. Comput. Modelling 36 (1–2), 121–127.

Delhez, E.J.M., Campin, J.-M., Hirst, A.C., Deleersnijder, E., 1999. Toward a general theory of the age in ocean modelling. Ocean Model. 1 (1), 17–27.

Denamiel, C., Budgell, W.P., Toumi, R., 2013. The Congo River plume: Impact of the forcing on the far-field and near-field dynamics. J. Geophys. Res. Oceans 118, 964–989.

Du, J., Park, K., Shen, J., Dzwonkowski, B., Yu, X., Yoon, B.I., 2018. Role of baroclinic processes on flushing characteristics in a highly stratified estuarine system, Mobile Bay, Alabama. J. Geophys. Res. Oceans 123 (7), 4518–4537.

Dupra, V., Smith, S.V., Marshall Crossland, J.I., Crossland, C.J., 2001. Estuarine systems of Sub-Saharan Africa: Carbon, nitrogen and phosphorus fluxes. LOICZ Rep. Stud. 18.

Duquesne, F., Vallaeys, V., Vidaurre, P.J., Hanert, E., 2021. A coupled ecohydrodynamic model to predict algal blooms in Lake Titicaca. Ecol. Model. 440, 109418.

Egbert, G.D., Erofeeva, S.Y., 2002. Efficient inverse modeling of barotropic ocean tides. J. Atmos. Ocean. Technol. 19 (2), 183–204.

Eisma, D., 1990. Station Report Zaire Estuary Cruise R.V. TYro 21/11-12/12/1989. NIOZ, Texel.

Eisma, D., Kalf, J., 1984. Dispersal of Zaire river suspended matter in the estuary and Angola basin. Netherlands J. Sea Res. 17 (2–4), 385–411.

Eisma, D., Kalf, J., van der Gaast, .S.J., 1978. Suspended matter in the Zaire estuary and the adjacent Atlantic. Netherlands J. Sea Res. 12 (3/4), 382–406.

Eisma, D., van Bennekom, .A.J., 1978. The Zaire River and estuary and the Zaire outflow in the Atlantic Ocean. Netherlands J. Sea Res. 12 (3/4), 255–272.

Feely, R.A., Alin, S.R., Newton, J., Sabine, C.L., Warner, M., Devol, A., Krembs, C., Maloy, C., 2010. The combined effects of ocean acidification, mixing, and respiration on pH and carbonate saturation in an urbanized estuary. Estuar. Coast. Shelf Sci. 88 (4), 442–449.

Geuzaine, C., Remacle, J.-F., 2009. Gmsh: A 3-D finite element mesh generator with built-in pre- and post-processing facilities. Internat. J. Numer. Methods Engrg. 79 (11), 1309–1331.

Geyer, W.R., MacCready, P., 2014. The Estuarine Circulation. Annu. Rev. Fluid Mech. 46 (1), 175–197.

Geyer, W.R., Ralston, D.K., 2011. The dynamics of strongly stratified estuaries. In: Wolanski, E., McLusky, D. (Eds.), Treatise on Estuarine and Coastal Science. Academic Press, pp. 37–51.

Goosse, H., Campin, J.-M., Tartinville, B., 2001. The sources of Antarctic bottom water in a global ice–ocean model. Ocean Model. 3 (1–2), 51–65.

Gourgue, O., Deleersnijder, E., White, L., 2007. Toward a generic method for studying water renewal, with application to the epilimnion of Lake Tanganyika. Estuar. Coast. Shelf Sci. 74 (4), 628–640.

Gräwe, U., Holtermann, P., Klingbeil, K., Burchard, H., 2015. Advantages of vertically adaptive coordinates in numerical models of stratified shelf seas. Ocean Model. 92, 56–68.

Haine, T.W.N., Hall, T.M., 2002. A generalized transport theory: Water-mass composition and age. J. Phys. Oceanogr. 32 (6), 1932–1946.

Hamilton, P., 1990. Modelling salinity and circulation for the Columbia River Estuary. Prog. Oceanogr. 25 (1), 113–156.

Haney, R.L., 1991. On the pressure gradient force over steep topography in sigma coordinate ocean models. J. Phys. Oceanogr. 21 (4), 610–619.

Hansen, D.V., Rattray, M., 1966. New dimensions in estuary classification. Limnol. Oceanogr. 11 (3), 319–326.

Hirst, A.C., 1999. Determination of water component age in ocean models: Application to the fate of North Atlantic Deep Water. Ocean Model. 1 (2–4), 81–94.

Hofmeister, R., Beckers, J.-M., Burchard, H., 2011. Realistic modelling of the exceptional inflows into the central Baltic Sea in 2003 using terrain-following coordinates. Ocean Model. 39 (3), 233–247.

Hofmeister, R., Burchard, H., Beckers, J.-M., 2010. Non-uniform adaptive vertical grids for 3D numerical ocean models. Ocean Model. 33 (1), 70–86.

Hopkins, J., Lucas, M., Dufau, C., Sutton, M., Stum, J., Lauret, O., Channellière, C., 2013. Detection and variability of the Congo River plume from satellite derived sea surface temperature, salinity, ocean colour and sea level. Remote Sens. Environ. 139, 365–385.

Ittekott, V., 1988. Global trends in the nature of organic matter in river suspensions. Nature 332 (6163), 436–438.

Kärnä, T., Baptista, A.M., 2016a. Evaluation of a long-term hindcast simulation for the Columbia River estuary. Ocean Model. 99, 1–14.

Kärnä, T., Baptista, A.M., 2016b. Water age in the Columbia River estuary. Estuar. Coast. Shelf Sci. 183, 249–259.

Kärnä, T., Legat, V., Deleersnijder, E., 2013. A baroclinic discontinuous Galerkin finite element model for coastal flows. Ocean Model. 61, 1–20.

Karstensen, J., Stramma, L., Visbeck, M., 2008. Oxygen minimum zones in the eastern tropical Atlantic and Pacific oceans. Prog. Oceanogr. 77 (4), 331–350.

Lambrechts, J., Comblen, R., Legat, V., Geuzaine, C., Remacle, J.-F., 2008. Multiscale mesh generation on the sphere. Ocean Dyn. 58 (5), 461–473.

Le Bars, Y., Vallaeys, V., Deleersnijder, E., Hanert, E., Carrere, L., Channellière, C., 2016. Unstructured-mesh modeling of the Congo river-to-sea continuum. Ocean Dyn. 66 (4), 589–603.

Legrand, S., Deleersnijder, E., Delhez, E.J.M., Legat, V., 2007. Unstructured, anisotropic mesh generation for the Northwestern European continental shelf, the continental slope and the neighbouring ocean. Cont. Shelf Res. 27 (9), 1344–1356.

Li, J.-X., Li, Y.-Y., Wang, B., 2016. Pressure gradient errors in a covariant method of implementing the σ-coordinate: idealized experiments and geometric analysis. Atmospheric Ocean. Sci. Lett. 9 (4), 270–276.

Liu, R., Zhang, X., Liang, B., Xin, L., Zhao, Y., 2017. Numerical study on the influences of hydrodynamic factors on water age in the Liao River estuary, China. J. Coast. Res. 80, 98–107.

Lucas, L.V., Deleersnijder, E., 2020. Timescale methods for simplifying, understanding and modeling biophysical and water quality processes in coastal aquatic ecosystems: A review. Water 12 (10), 2717.

Meier, H.E.M., 2005. Modeling the age of Baltic Seawater masses: quantification and steady state sensitivity experiments. J. Geophys. Res. Oceans 110 (C2).

Monahan, D., 2008. Mapping the floor of the entire world ocean: the general bathymetric chart of the oceans. J. Ocean Technol. 3 (1), 108.

Paerl, H.W., Pinckney, J.L., Fear, J.M., Peierls, B.L., 1998. Ecosystem responses to internal and watershed organic matter loading: consequences for hypoxia in the eutrophying Neuse River Estuary, North Carolina, USA. Mar. Ecol. Prog. Ser. 166, 17–25.

Pak, H., Zaneveld, J.R.V., Spinrad, R.W., 1984. Vertical distribution of suspended particulate matter in the Zaire river, estuary and plume. Netherlands J. Sea Res. 17 (2), 412–425.

Paulmier, A., Kriest, I., Oschlies, A., 2009. Stoichiometries of remineralisation and denitrification in global biogeochemical ocean models. Biogeosciences 6 (5), 923–935.

Phillipson, L., Toumi, R., 2017. Impact of data assimilation on ocean current forecasts in the Angola Basin. Ocean Model. 114, 45–58.

Phillipson, L., Toumi, R., 2019. Assimilation of satellite salinity for modelling the Congo River plume. Remote Sens. 12 (1).

Rayson, M.D., Gross, E.S., Hetland, .R.D., Fringer, O.B., 2016. Time scales in Galveston Bay: An unsteady estuary. J. Geophys. Res. Oceans 121 (4), 2268–2285.

Rutherford, K., Fennel, K., 2018. Diagnosing transit times on the northwestern North Atlantic continental shelf. Ocean Sci. 14 (5), 1207–1221.

Savoye, B., Babonneau, N., Dennielou, B., Bez, M., 2009. Geological overview of the Angola-Congo margin, the Congo deep-sea fan and its submarine valleys. Deep-Sea Res. II 56, 2169–2182.

Shchepetkin, A.F., McWilliams, J.C., 2005. The regional oceanic modeling system (ROMS): a split-explicit, free-surface, topography-following-coordinate oceanic model. Ocean Model. 9 (4), 347–404.

Shepard, F.P., Emery, K.O., 1973. Congo submarine canyon and fan valley. AAPG Bull. 57 (9), 1679–1691.

Spencer, R., Hernes, P., Aufdenkampe, A., Baker, A., Gulliver, P., Stubbins, A., Aiken, G.R., Dyda, R., Butler, K., Mwamba, V., Mangangu, A., Wabakanghanzi, J., Six, J., 2012. An initial investigation into the organic matter biogeochemistry of the Congo River. Geochimica Et Cosmochimica Acta 84, 614–627.

Spencer, R.G.M., Stubbins, A., Gaillardet, J., 2013. Geochemistry of the congo river, estuary, and plume. In: Bianchi, M.A., Cai, W.-J. (Eds.), Biogeochemical Dynamics At Major River-Coastal Interfaces: Linkages with Global Change. Cambridge University Press, pp. 554–583.

Vallaeys, V., Kärnä, T., Delandmeter, P., Lambrechts, J., Baptista, A.M., Deleersnijder, E., Hanert, E., 2018. Discontinuous Galerkin modeling of the Columbia River's coupled estuary-plume dynamics. Ocean Model. 124, 111–124.

Vangriesheim, A., Pierre, C., Aminot, A., Metzl, N., Baurand, F., Caprais, J.-C., 2009. The influence of congo river discharges in the surface and deep layers of the Gulf of Guinea. Deep-Sea Res. Part II: Trop. Stud. Oceanogr. 56, 2183–2196.

Vieira, L.H., Krisch, S., Hopwood, M.J., Beck, A.J., Scholten, J., Liebetrau, V., Achterberg, E.P., 2020. Unprecedented Fe delivery from the Congo River margin to the South Atlantic Gyre. Nature Commun. 11 (1), 1–8.

White, L., Legat, V., Deleersnijder, E., 2008. Tracer conservation for three-dimensional, finite-element, free-surface, ocean modeling on moving prismatic meshes. Mon. Weather Rev. 136 (2), 420–442.

White, R.H., Toumi, R., 2014. River flow and ocean temperatures: The Congo River. J. Geophys. Res. Oceans 119 (4), 2501–2517.

Yang, J., Kong, J., Tao, J., 2019. Modeling the water-flushing properties of the Yangtze estuary and adjacent waters. J. Ocean University of China 18 (1), 93–107.

Zhang, Y.J., Ateljevich, E., Yu, H.-C., Wu, C.H., Yu, J.C.S., 2015. A new vertical coordinate system for a 3D unstructured-grid model. Ocean Model. 85, 16–31.